Sustainable Energy & Fuels

Interdisciplinary research for the development of sustainable energy technologies

Accepted Manuscript

This article can be cited before page numbers have been issued, to do this please use: S. Murcia-López, M. Chakraborty, N. M. Carretero, C. Flox, J. R. Morante and T. Andreu, *Sustainable Energy Fuels*, 2019, DOI: 10.1039/C9SE00949C.

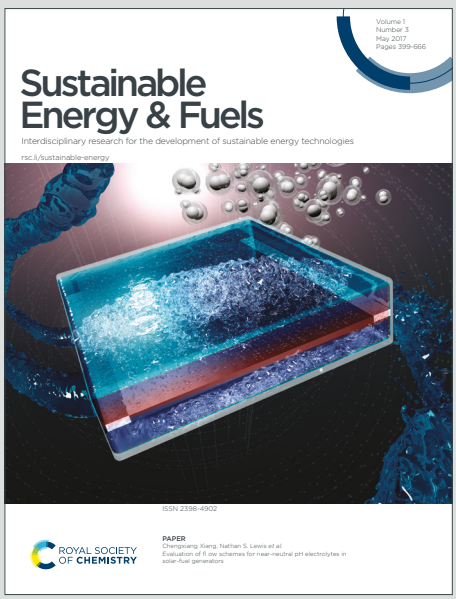

View Article Online
DOI: 10.1039/C9SE00949C

ARTICLE

Adaptation of Cu(In, Ga)Se_2 Photovoltaics for Full Unbiased Photocharge of Integrated Solar Vanadium Redox Flow Batteries

Received 00th January 20xx,
Accepted 00th January 20xx

DOI: 10.1039/x0xx00000x

Sebastián Murcia-López,*[a] Monalisa Chakraborty,[a] Nina M. Carretero,[a] Cristina Flox,[a] Joan Ramón Morante[a,b] and Teresa Andreu [a]

The integration of photovoltaics and vanadium redox flow batteries (VRFB) is a promising alternative for the direct conversion and storage of solar energy in a single device, considering their inherent higher energy density versus other redox pairs. However, this integration is not seamless unless the photovoltaic system is customized to the voltage needs of the battery, which unlike artificial photosynthesis, continuously increase with the state-of-charge. We have developed integrated solar VRFB with adapted low-cost Cu(In, Ga)Se_2 modules of 3 and 4 series-connected cells (solar efficiency of mini-solar module 8.1%), and considering the voltage requirements (1.3-1.6V), we have evaluated the influence of the photovoltaic operation region on the final efficiency of the solar VRFB. Full unbiased photocharge under 1 Sun illumination has been achieved reaching high energy (77%), solar-to-charge (7.5%) and overall round trip energy conversion efficiencies (5.0%) excelling the values reported in literature for other solar VRFB, thus demonstrating the feasibility and intrinsic potential of adapting low-cost commercial photovoltaics to such energy storage systems.

Introduction

The current progress in photovoltaics (PV) technology has led solar energy to be foreseen as the foremost source of renewable energy in a decarbonized long-term scenario. Still, the development of more efficient systems faces the intermittency inherent to sunlight and mismatching between production and demand as crucial limitations.[1] In this context, the integration of PV and energy storage systems such as batteries is an appealing approach that pursues simplification through direct conversion and storage of solar into (electro)chemical energy. These so-called solar batteries offer the advantage of carrying out in a single device, a process normally done in several independent units.[2,3] The historical development of photoelectrochemical (PEC) storage devices shows, however, that this is not a recent approach.[4] Between late 1970s to late 1980s, many PEC approaches using organic and inorganic redox-pairs in stagnant configurations were developed, mostly with photoelectrodes in direct contact with the electrolyte and based on metal oxides, chalcogenides and III-V semiconductors. Despite some systems demonstrated impressive efficiency values (e.g., solar-to-electrical energy conversion efficiency of 11.8%),[5] relevant aspects such as limited availability of low-cost and efficient photo-absorbers and membranes, notably restrained the interest on these approaches at the time. Over the last few years, with the progress on PV technology and electrochemical devices (with more efficient and cheaper membranes and cells) this possibility has re-gained attention, with configurations aiming to create compact and cost-effective devices by integrating PV materials or developing photoelectrodes in systems such as lithium-ion[6] and redox flow batteries (RFB). The last ones, in particular, are probably the most seamless integration alternative, considering their advantages such as decoupling of power and energy capacity, long cycle life and scalability. [7,8] More importantly, these systems possess analogous versatility than the initial stagnant PEC storage approaches, with the possibility of combining different redox pairs. In fact, some of the newest solar RFB have re-introduced organic and inorganic species used in the 1980s PEC systems.[4] For instance, the iodide/polyiodide pair also used in the dye-sensitized solar cell (DSSC) technology has led to the development of integrated systems with DSSCs based on iodine catholytes, and anolytes such as lithium [9] or decamethylferrocene.[10] These systems, however, are limited by the performance of the TiO_2 photoanodes. More recently, quinones/halogens RFB with relative low cell potential (~0.8 V) have also appeared as examples of successful solar RFB, by using photoelectrodes based on Si,[11] DSSC[12] or WSe_2,[13] although the intrinsic cell potential limits their discharge power. A more recent example of higher voltage battery has been proposed by Wang and co-authors[14] with a ferrocyanide/anthraquinone battery with

[a] Catalonia Institute for Energy Research (IREC), Jardins de les Dones de Negre 1, Sant Adrià de Besós, 08930, Spain.
[b] University of Barcelona (UB), Martí i Franquès 1, Barcelona, 08020, Spain.
* Corresponding author:
E-mail: smurcia@irec.cat.

Electronic Supplementary Information (ESI) available: detailed mini-modules preparation, comparative of fabrication cost for different thin film PV, galvanostatic measurements, estimated battery efficiencies, i-V curves of the CIGS modules, solar cell efficiencies, cell voltage and photocurrent variation during photocharge tests. See DOI: 10.1039/x0xx00000x

integrated Ta_3N_5 photoanode and GaN/Si photocathode reaching 1.2 V and operating under static conditions.

Compared to other RFB, all-vanadium redox flow batteries (VRFB), which emerged in 1986, have minimized crossover effects[15,16] and display higher power density considering their standard cell potential of 1.26 V, reaching values of up to 1.7 V in real operation,[17] but also represent a more challenging approach for PV integration. Despite this, they have already demonstrated to be suitable energy storage systems for renewable solar and wind energy, even with power output fluctuations of the renewable system.[17,18] Actually, a CdS/DSSC photoanode proposed by Azevedo et al., and a monolithic triple junction solar cell proposed by Urbain et al., are up to now the only examples of integrated systems in full VRFB,[21,22] as the other studies on solar VRFB have used TiO_2 photoelectrodes, reaching limited state-of-charge (SoC) or providing photo-assisted charge under low bias conditions.[23,24]

Chalcopyrites Cu(In, Ga)Se_2 (CIGS) light absorbers are a promising alternative among other thin-film PV technologies[25] and even to crystalline silicon, given their higher absorption coefficient that allows using less amount of active material.[26,27] Therefore, CIGS-based PV has been commercialized and become more cost competitive (see Table S1 for comparison with other technologies) with efficiency values of ~16% (world record higher than 20%)[1,25,28] and an additional advantage: CIGS can be directly grown on flexible substrates like metal foils, which can facilitate the integration into electrochemical cells. Moreover, several works on photoelectrochemical water splitting using CIGS[29,30] are good examples of how they can be properly customized to solar VRFB. In fact, recently Bae et al. theoretically correlated several parameters on solar RFB with single photo-absorbers and found that with low electrolyte resistance, commercial PV materials such as c-Si, GaAs and CIGS are promising alternatives.[31] Though, this is not a straightforward task: for achieving unbiased photocharge, the PV must properly match the energy requirements of the VRFB, considering also that the cell voltage varies with the SoC following a Nernstian behavior (equation 1), while the overpotential available for photocharge (or the photocurrent) decreases at high SoC.[4] Therefore, unlike systems coupling PV and energy storage systems counting with power electronics units for tracking the PV maximum power point (MPP) and controlling the charge of the battery, the main challenge to be solved for the integrated system is matching the PV MPP and the RFB considering the inherent potential shift of the latter.[2] This is a critical aspect at high SoC, especially in systems with single photoabsorbers,[31] but must be carefully considered even in devices using two photoelectrodes or PV configurations with tandem or multijunction approaches. A good example on this aspect has been addressed by Li et al.,[32] for an integrated system with organic redox pairs and a III-V tandem solar cell (with PV efficiency of 26.1%), reaching a record efficiency of 14.1%. Despite the promising value attained, an intrinsic loss of 0.6 V photovoltage deriving in undesired efficiency loss compared to the solar cell efficiency evinces the need for proper matching. Very recently, an organic solar RFB based on viologen- and ferrocene-derived redox couples with c-Si photoelectrodes has achieved a promising stable performance and solar round-trip energy efficiency of 5.4%,[33] attributed to the proper matching between the photoelectrodes and the redox pairs, moving a step forward into the development of more efficient systems.

Based on this, we have carried out the integration of adapted CIGS (as "embedded" photoelectrodes) into VRFB without additional power electronics (Figure 1), by evaluating two mini-modules fabricated from commercial thin film PV, in two different battery configurations (symmetric V4/V4 and asymmetric V4/V3). These systems reach full unbiased photocharge with high overall round trip energy conversion efficiencies. Moreover, the two adapted modules have shown to work at different power regions, so that we have also assessed the influence of different charging conditions (constant and variable charge power) on the final performance of the solar VRFB. This work aims to develop integrated "embedded" minimodules by using thin film photovoltaics, adapted for fitting the specific requirements of the battery. Based on the intrinsic higher voltage requirements of VRFB, two battery configurations and two multijunctions of 3 and 4 solar cells were successfully integrated, achieving proper matching of the operating conditions during photo-charge. Ultimately this approach opens the path to further real development of such systems by following relatively simple approaches, even starting with commercial photovoltaics.

Experimental part

CIGS PV module preparation. Thin film photovoltaics based on $CuInGaSe_2$ (CIGS) supported on stainless steel was purchased from SoloPower®. For the preparation of the PV modules, the commercial CIGS foil was cut into small cells of 5.1-5.3 cm^2 geometric area, after which the borders were etched with 0.5M H_2SO_4 to dissolve the metal oxides and eliminate electrical shunts. The series-connected photovoltaic cells were wired with a conductive Cu sheet and Ag electrically conductive transfer tape (ECATT 9703, 3MTM). Hence, 3- and 4-cells PV modules (namely, 3CM and 4CM) were prepared, attaining different open circuit potential and current density. The PV modules were sealed to avoid the contact with the electrolyte, with Optically Clear Double-Sided Adhesive Tape (THORLABS) and kapton® adhesive tape (Dupont). A scheme depicting the different steps is included in Figure S1. The final geometric areas of the 3CM and 4CM were 16 and 20.4 cm^2. The i-V characteristic curves of the CIGS modules were recorded at 30 $mV \cdot s^{-1}$ using a VMP3 BioLogic Potentiostat and a PEC-L01 solar simulator (PECCELL Technologies, Inc) with AM 1.5G filter and 1 Sun irradiation.

Preparation of carbon electrodes. Rayon-based carbon Felt (CF) with 6 mm of thickness was purchased from Mersen. A plasma etching process under O_2 atmosphere was carried out as pre-treatment prior to TiO_2 deposition and/or assembling into the electrochemical cell. For the negative side, hydrogenated TiO_2-CF electrodes (H-TiO_2/CF) were prepared

by following a previously reported hydrothermal procedure for depositing rutile nanorods,[34] which were further hydrogenated by means of a thermal treatment under H_2/Ar atmosphere. These electrodes have previously shown a good performance for the V^{3+}/V^{2+} side reaction in VRFB, associated to the combination of: i) higher surface hydroxylation leading to a higher presence of actives sites for V^{3+} reduction, ii) HER inhibition, and iii) partial hydrogenation improving the charge transfer at the electrode/electrolyte interface.[34] On the positive side, O_2-plasma etched carbon felts were used. The geometric area of the electrodes was 10 cm^2.

Full VRFB tests. The photo-assisted charge/ discharge tests were performed in an adapted electrochemical cell with a Poly(methyl methacrylate) (PMMA) window on one side, two graphite plates as current collectors (Electrocell), a Nafion® 117 membrane (pre-treated in 3% H_2O_2, H_2O and 0.5M H_2SO_4 at 80ºC) and the carbon felt electrodes on the corresponding compartment. The electrolyte flow was driven by peristaltic pumps (Major Science, MU-D02) with a volumetric flow rate of 13 mL·min^{-1} and an estimated linear flow velocity of ~8.1 cm·min^{-1}, for a 16% felt compression and a porosity of 0.8 (under compression). The "embedded" CIGS module was integrated by coupling on the negative side of the cell, between the PMMA window and the graphite current collector. Additionally a reference electrode (Ag/AgCl) was inserted into the negative side of the cell and the individual potentials vs reference were followed during tests (Figure 1A). The individual potentials have been referred to the standard hydrogen electrode (SHE) by means of the expression: $V_{SHE} = V_{Ag/AgCl} + 0.059 \cdot pH + 0.199V$.

Before performing the (photo)charge/discharge experiments, the V^{3+} anolyte was electrogenerated through a galvanostatic charge (30 mA·cm^{-2}) using 0.5M $VOSO_4$ in 3M H_2SO_4 electrolyte on both sides (twice the volume of catholyte than anolyte), after which V^{2+} and VO_2^+ were obtained in the negative and positive sides, respectively. Afterwards, half of the volume was extracted from the catholyte and a galvanostatic discharge (30 mA·cm^{-2}) was performed in order to obtain V^{3+} and VO^{2+} as starting catholyte and anolyte for the (photo)charge/discharge tests. Different volumes in the range of 7.5-15 mL in each compartment were used during the different tests.

Prior to the photo-assisted tests and in order to validate the effective performance of the cell, the full VRFB was tested under galvanostatic conditions, by means of charge/discharge cycles at two current densities: 10 and 20 mA·cm^{-2} (see SI for more information). Finally, an additional test by charging up to several SoC values and measuring linear scan voltammetries (LSV) in two-electrode configuration at 40 mV·s^{-1} were carried out.

During the photocharge experiment, the CIGS modules were illuminated at 0 V conditions with a PEC-L01 solar simulator (PECCELL Technologies, Inc) equipped with a 300W Xe arc lamp and AM 1.5G filter. A cross-sectional view with the PV minimodule configuration and the electron transfer to the anolyte can be found in Figure 1B. The irradiance was adjusted to 100 mW·cm^{-2} (1 Sun) using a silicon diode (XLPF12-3S-H2-DO; Gentec-EO). Both the photocurrent generated at the PV system and the open circuit potential in the cell were followed with a VMP3 BioLogic potentiostat.

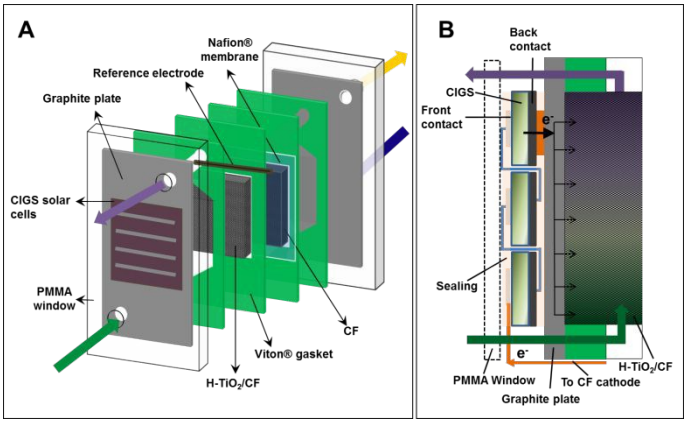

Figure 1. Scheme of the integrated solar VRFB with the CIGS solar cells (A). The cell was assembled with a reference electrode in the negative side, close to the H-TiO_2/CF. Cross-sectional view (B) of the electron transfer between the PV minimodule and the anode side.

Although the potential depends on specific conditions such as temperature and concentration of active species, in general terms, the cell voltage in VRFB vary between 1-1.55 V from the thermodynamic point of view and as predicted by the Nernst equation (equation 1), where c_X is the given concentration of the ions involved in the overall reaction in the positive and negative sides, F is the Faraday constant, n is the number of electrons exchanged in the reaction, T is the temperature and R is universal gas constant. Under real operation these values are expected to increase because of intrinsic overpotential and ohmic losses.

$$E = E^0 + \frac{RT}{nF}\ln\left[\frac{c_{VO_2^+} \cdot c_{V^{2+}} \cdot c_{H^+}^2}{c_{VO^{2+}} \cdot c_{V^{3+}}}\right] \qquad (1)$$

Therefore, after reaching OCP values of 1.5-1.6V and by considering the theoretical charge capacity and the coloration of the electrolytes, the battery was considered fully charged, the illumination was stopped and the galvanostatic discharge at a selected current density was carried out up to a cell voltage limit of 0.7 V, corresponding to a fully discharged battery under our established conditions.

V4/V4 VRFB test. Several solar rechargeable flow batteries have been already proposed in literature, combining different vanadium species which adapt the overall redox potential to the photovoltage provided by the photoactive material. In particular, symmetrical configurations such as VO_2^+,VO^{2+} ‖ VO^{2+},V^{3+} (V4/V4) and VO^{2+},V^{3+} ‖ V^{3+},V^{2+} have been successfully photocharged with TiO_2 [20] and CdS/CdSe materials.[21] Though, these battery configurations do not possess the overall potential than the full VO_2^+,VO^{2+} ‖ V^{3+},V^{2+} VRFB, as seen by reactions in equations 2-4 and 5-7:

View Article Online
DOI: 10.1039/C9SE00949C

$$VO_2^+ + 2H^+ + e^- \leftrightarrow VO^{2+} + H_2O \quad E^0 = 1.0\ V_{SHE} \quad (2)$$

$$V^{2+} \leftrightarrow V^{3+} + e^- \quad E^0_{V^{3+}/V^{2+}} -0.26\ V_{SHE} \quad (3)$$

Overall Full VRFB:

$$VO_2^+ + 2H^+ + V^{2+} \leftrightarrow VO^{2+} + H_2O + V^{3+} \quad E^0 = 1.26 V_{SHE} \quad (4)$$

$$VO_2^+ + 2H^+ + e^- \leftrightarrow VO^{2+} + H_2O \quad E^0 = 1.0 V_{SHE} \quad (5)$$

$$V^{3+} + H_2O \leftrightarrow VO^{2+} + 2H^+ + e^- \quad E^0_{VO^{2+}/V^{3+}} = 0.34\ V_{SHE} \quad (6)$$

Overall V4/V4 battery:

$$VO_2^+ + V^{3+} \leftrightarrow 2VO^{2+} \quad E^0 = 0.66\ V_{SHE} \quad (7)$$

Besides the measurements performed under normal conditions with a full VRFB (V3/V4), a preliminary test with a symmetrical configuration by using the same parent active species on both sides (VO^{2+}, namely V4/V4) was carried out with the 3CM module. In this kind of RFBs, the same parent molecule is oxidized and reduced on each half-cell.[35,36] Thus, the charge parameters were evaluated by following the same photocharge procedure: initially 10 mL of fresh VO^{2+} electrolytes (0.5 M $VOSO_4$ in 3M H_2SO_4) were added into each compartment (without electrogeneration), after which the PV was illuminated under the same conditions that in the full cell test. This way, the thermodynamic overall cell voltage decreased to around 0.66 V and the photocharge was completed after obtaining V^{3+} and VO_2^+ in the negative and positive reaction side, respectively.

Efficiency calculation. The fill factor (FF) and the solar cell efficiency (η) of the CIGS PV modules were estimated according to equations 8-9:

$$FF = \frac{I_{max} \cdot V_{max}}{I_{SC} \cdot V_{OC}} \quad (8)$$

$$\eta = \frac{V_{OC} \cdot I_{SC} \cdot FF}{P_{in}} \quad (9)$$

Where, I_{max} and V_{max} are the photocurrent and photovoltage at the maximum power point, V_{OC} and I_{SC} are the open circuit voltage and the short circuit current, respectively, and P_{in} is the incident solar power.

On the other hand, the VRFB efficiencies were determined from the (photo)charge/discharge curves. Coulombic (CE), voltage (VE) and energy (EE) efficiencies were calculated by following equations 10-12.

$$CE = \frac{Q_{discharge}}{Q_{photocharge}} = \frac{\int i_{discharge} dt}{\int j_{photocharge} dt} \quad (10)$$

$$VE = \frac{V_{discharge}}{V_{photocharge}} \quad (11)$$

$$EE = CE \cdot VE \quad (12)$$

Where *Q* is the battery capacity obtained from the integration of the current curve with time, and *V* is the average cell potential during charge/discharge. The specific capacity was calculated by dividing Q by the total electrolyte volume in the two compartments. Despite the difference in the conditions between the photocharge and the discharge (i.e. drop of the photocurrent density during photocharge versus the constant current during discharge, especially with the 3CM), coulombic, voltage and energy efficiencies were estimated for comparison.

The electrolyte utilization was defined as the ratio between the capacity attained during discharge ($Q_{discharge}$) and the maximum theoretical capacity ($Q_{theoretical}$) according to the concentration and volume of active species in the electrolyte on both compartments.

In general, although V_{OC} and OCP represent the open-circuit voltage, the former was referred to the PV, and the latter, to the VRFB.

A solar-to-charge efficiency (η_{STC}) was calculated as the ratio between the energy stored and the incident energy during the photocharge. Obviously, the instantaneous η_{STC} changes with the SoC, and a general expression can be found in equation 13:

$$\eta_{STC} = \frac{E_{charge}}{E_{in}} = \frac{Q_{photocharge} \cdot V_{photocharge}}{A \cdot P_{hv} \cdot t} \times 100\% \quad (13)$$

Where $Q_{photocharge}$ is the battery capacity during photocharge (mA·h), $V_{photocharge}$ is the average charge potential (V), *A* is the area of the photovoltaic module (cm^2), P_{hv} is the incident illumination power density ($mW \cdot cm^{-2}$) and *t* is the charge time (h). The variation of the instantaneous value was also calculated for the solar VRFB with the two minimodules.

The overall round trip energy conversion efficiency (η_{RT}) can be expressed as the ratio between the total energy extracted from the system and the energy supplied during the charge (i.e. incident photon energy) can be calculated as expressed in equation 14:

$$\eta_{RT} = \frac{E_{out}}{E_{in}} = \frac{Q_{discharge} \cdot V_{discharge}}{A \cdot P_{hv} \cdot t} \times 100\% \quad (14)$$

Where $Q_{discharge}$ is the battery capacity during discharge (mA·h) and $V_{discharge}$ is the average discharge potential (V).

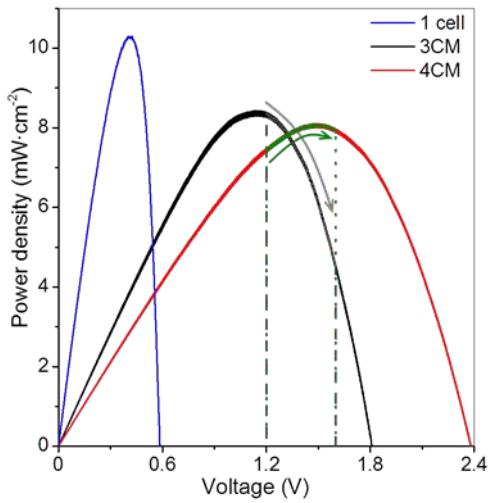

Figure 2. P-V curves of the CIGS modules under 1 Sun illumination. The marked areas indicate the voltage window during the photocharging step.

Results and Discussion

CIGS characterization. The single selected CIGS cell displays V_{OC} of 0.6 V and short circuit current of 35 mA·cm^{-2} (Figure S3), leading, in our case, to estimated solar cell efficiency of 10.3%. Considering these values and the cell voltages observed in the charge-discharge cycling of the VRFB, we determined that modules of at least 3 or 4 series-connected cells (namely 3CM and 4CM) were necessary for full unbiased photocharge. As seen in the i-V curves in Figure S3, we obtained the expected V_{OC} values: 1.8 and 2.4 V for the 3 and 4-cell modules, respectively (Table S3). However, slightly lower fill factors were obtained and the solar cell efficiencies in the multijunctions decreased to around 8.4-8.1%. This can be attributed to additional shunt resistances introduced during the preparation of the modules. Alternative interconnection strategies such as monolithic interconnection[23] could probably lead to better solar cell efficiencies than the tabbing method used in the present work. Despite the V_{OC} values of the series-connected modules are high enough to accomplish the unbiased photocharge, it is also necessary to consider the potential variation of the battery cell voltage with the SoC, leading to a constant shift in the operation point of the PV system as shown in Figure 2. The significant photocurrent decrease (Figure S3) in the 3CM (from 21% in the 4CM to around 59% in the 3CM) clearly illustrates that the operation point in this system is not the optimum, so that probably might limit the photocharge of the VRFB.

3CM evaluation: V4/V4 and full VRFB. As proof of concept, the 3CM was first evaluated in a RFB with symmetrical VO_2^+,VO^{2+} ‖ VO^{2+},V^{3+} (V4/V4) configuration, because of the lower standard redox potential between these two vanadium pairs (E^0 = 0.66 V, equation 7).[35] For this purpose, the same starting VO^{2+} electrolyte was used in both compartments. The charge profile and the photocurrent density are shown in Figure 3A. The full charge was completed after ~2.3 h of illumination, as indicated by the steep increase in the cell potential. At this point, the irradiation was stopped and the system was led at open-circuit, reaching ~0.8 V. Besides the color change of the electrolytes, the calculated capacity attained under photocharge (~6700 mA·h·L^{-1}) indicates a SoC of around 98.5% was reached (namely, VO^{2+} and V^{3+} formed in the positive and negative sides, respectively). Therefore, the suitability of the 3CM for unbiased photocharge of the V4/V4 system was demonstrated, although certainly this configuration has limited practical interest given its lower energy density versus a full VRFB. Additionally, further optimization for specific reaction kinetics (in particular for the V^{3+}/VO^{2+} half-reaction) would be necessary, as seen by the relative high charge overpotential observed in this system, and probably justified by the use of an electrode enhanced for the V^{3+}/V^{2+} reactions on the anode side.

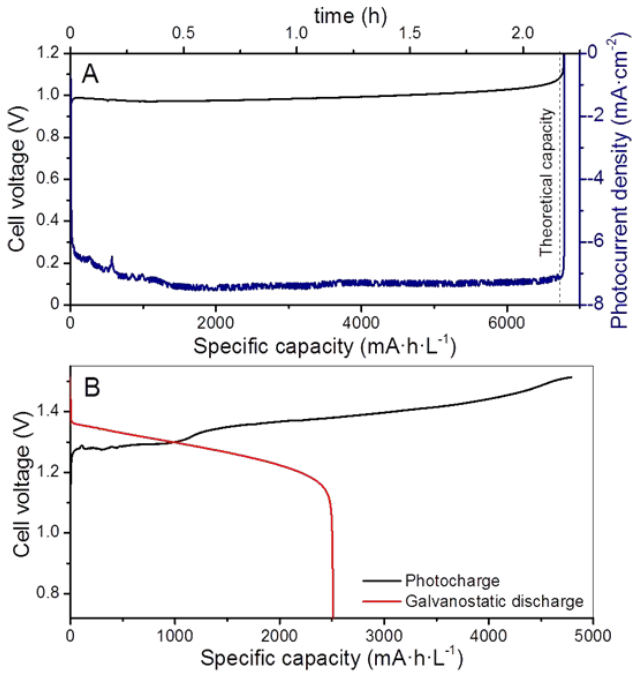

Figure 3. 3CM results: photocurrent density and cell voltage evolution during the unbiased photocharge of the integrated V4/V4 configuration (A). Photocharge/discharge curves of the full VRFB configuration (B). The galvanostatic discharge was carried out at 10 mA·cm^{-2} (per CF area).

Once the V4/V4 configuration was assessed, the electrolytes were substituted by fresh VO^{2+} and V^{3+} solutions in the catholyte and anolyte, respectively, in a regular full VRFB configuration. The cell was assembled as described in Figure 1 and a photocharge/discharge was evaluated. As seen in Figure S4, the variation of the cell potential during the photocharge remarkably matches the photocurrent of the PV system, which continuously drops with time as the SoC (i.e., cell potential) increases. The cell voltage slowly increased until reaching 1.5 V (Figure 2B) and remained practically constant afterwards, with a photocurrent below 1.0 mA·cm^{-2}. After having a photocurrent of 0.5 mA·cm^{-2} with a cell voltage of ~1.52V, and considering the slow capacity increase (inset of Figure S4), the

photocharge was stopped and the galvanostatic discharge started.

The fact of not observing a steep increment in the cell potential suggests two features, at difference to the galvanostatic charge or to the photocharge with 4CM (as shown later): 1) the 3CM is not able to provide enough voltage for other parasitic reactions such as water splitting to occur, and 2) the photocurrent of the 3CM has such significant decrease after certain SoC, that the photocharge stops being effective and the overall cell potential (i.e. SoC) is not affected. Indeed, the galvanostatic discharge also reflects the difference between the photocharge and discharge capacities, deriving in poor coulombic and energy efficiencies (52 and 47%, respectively) and electrolyte utilization of only 37.5%.

An additional test with the 3CM at lower irradiation (50 $mW \cdot cm^{-2}$, in order to work at ~1 $mA \cdot cm^{-2}$) and by leaving the battery to fully attain the maximum charge capacity is shown in Figure S5. Despite reaching the theoretical capacity after more than 7 h of photocharge, the cell voltage remained lower than 1.4 V. Moreover, the battery only reaches half of capacity during discharge, with coulombic efficiency and electrolyte utilization of ~54%. Interestingly, the solar-to-charge (η_{STC}) and overall round trip energy conversion (η_{RT}) efficiencies[11,13] calculated for the battery with the integrated 3CM under both conditions show very similar values. This way, average η_{STC} and η_{RT} of 3.2 and 1.5-1.6% are respectively obtained, which, compared to the solar efficiency of 8.4%, evidences the limited power attained by the 3CM, inadequate for fully charging the VRFB. As observed in Figure 2, assembling the system with this module implies that the photocharge starts at the PV MPP and moves towards a lower power direction (patterned zone). Interestingly, the η_{STC} for the V4/V4 configuration with the 3CM leads to a higher value of 7.0%, demonstrating its suitability for photocharging a symmetrical V4/V4.

4CM evaluation in full VRFB. Considering the limited operation of the 3CM, the battery was assembled with the 4CM in full VRFB configuration. As seen in Figure 4, the photocurrent of the PV module slightly varied between 6-4 $mA \cdot cm^{-2}$, while the ones reached by the 3CM drastically dropped from 6 to 1 $mA \cdot cm^{-2}$. In fact, the profiles of the curves were more stable with this module and the cell potential steeply increased after reaching high SoC. This way, full photocharges were achieved, leading to capacities close to the theoretical value. Thereafter, the galvanostatic discharges were carried out, leading to discharge capacities of ~5000 $mA \cdot h \cdot L^{-1}$ as shown in Figure 5. In general, except for a minor imbalance observed during the first cycle, the battery shows a stable behavior during cycling, attaining very similar efficiencies and capacities with successive photocharges/discharges. Furthermore, the energy efficiency reached (77%) is similar to that of the galvanostatically charged VRFB (Table S4).

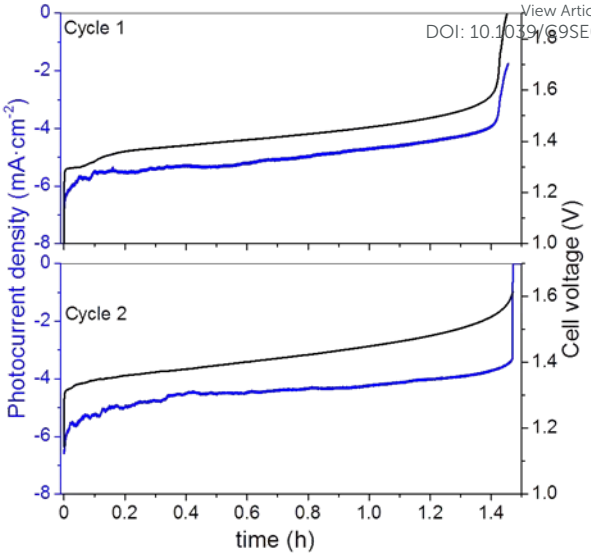

Figure 4. Variation of the photocurrent density and cell voltage during unbiased photocharge (cycles 1 and 2) with the 4CM.

As in the galvanostatic cycling (see SI), the individual electrode potentials in the positive (E_p) and negative (E_n) sides were simultaneously recorded by using a reference electrode (Figure S6A). A similar behavior is found regarding the evolution of the individual potentials of the galvanostatic charge/discharge: during photocharge, the E_p varies between 1.1-1.25 V_{SHE}, close the thermodynamic potential of the VO^{2+}/VO_2^+ redox reaction, and seems to more promptly increase after all the available VO^{2+} is oxidized, while the E_n steeply increases during discharge, after all the V^{2+} is re-oxidized to V^{3+}. These results suggest a minor imbalance also observed in the galvanostatic measurements, only related to the VRFB performance, rather than to the photovoltaics. However, as seen by the reached OCP of ~1.5 V and by the electrolyte coloration before and after photocharge (Figure S6B), both compartments reach a high SoC.

Additional comparison in terms of the power density gained during charge is included in Figure 6A, where we compare the (photo)charge with 3CM, 4CM and galvanostatic conditions. While the power density constantly increases in the galvanostatic charge operating at constant current with a concomitant voltage increase, the power density with the 3CM continuously decreases (the photocharge starts at the MPP) and the one by the 4CM remains almost constant before reaching high SoC. In the 4CM, the minor photocurrent decrease is compensated by the continuous increase of the cell voltage in the battery. Ultimately, the specific energy density during the photocharge with the 4CM is even higher than that of the galvanostatic charge (845 versus 887 $mW \cdot h \cdot cm^{-2} \cdot L^{-1}$). For comparison, the power density during V4/V4 experiment with the 3CM is also included, showing a constant value. Despite the lower power, explained by the lower cell voltage under this configuration, the 3CM again demonstrates to be suitable for photocharging a V4/V4 VRFB.

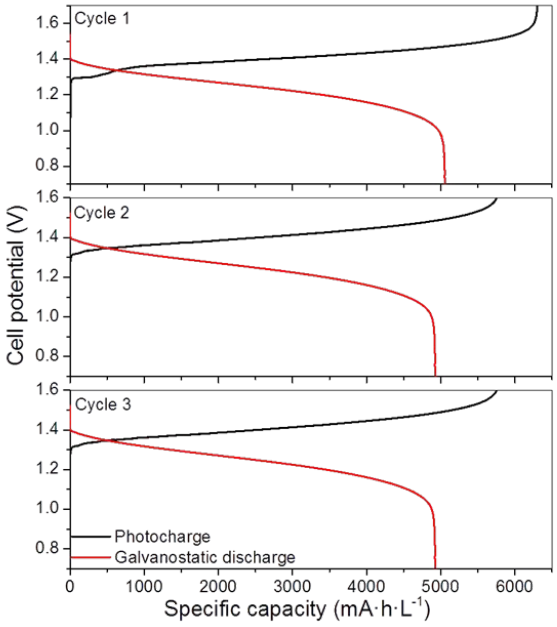

Figure 5. Photocharge/discharge curves of the VRFB with the 4CM. The galvanostatic discharge was carried out at 10 mA·cm^{-2} (5 mA·cm^{-2} per PV area).

Additional comparison in terms of the power gained during charge is included in Figure 6A, where we compare the (photo)charge with 3CM, 4CM and galvanostatic conditions. While the power constantly increases in the galvanostatic charge operating at constant current with a concomitant voltage increase, the power with the 3CM continuously decreases (the photocharge starts at the MPP) and the one by the 4CM remains almost constant before reaching high SoC. In the 4CM, the minor photocurrent decrease is compensated by the continuous increase of the cell voltage in the battery. Ultimately, the specific energy density during the photocharge with the 4CM is even higher than that of the galvanostatic charge (845 versus 887 mW·h·cm^{-2}·L^{-1}). For comparison, the power during V4/V4 experiment with the 3CM is also included, showing a constant value. Despite the lower power, explained by the lower cell voltage under this configuration, the 3CM again demonstrates to be suitable for photocharging a V4/V4 VRFB.

Linear scan voltammetries (LSV) were carried out to the battery at different SoC, and the comparison of the curves with the i-V of the two modules is shown in Figure 6B. At 0% SoC, the crossing point between the VRFB and the 3CM curves already overpasses the MPP of the PV, and a maximum photocurrent of 100 mA can be expected (~6.5 mA·cm^{-2} per PV area). For the 4CM, however, the MPP is not overpassed below a 75% SoC. This fact confirms that from the point of view of operation conditions, the 4CM properly matches the working voltage of the VRFB.

Besides the electrochemical efficiencies, we estimated the average η_{STC} at high SoC (for instantaneous evolution, see Figure S7) and η_{RT} for the 4CM, obtaining values of 7.5 and 5.0%, respectively. In particular, the η_{RT} obtained with the 4CM is, to our knowledge, among the highest values reached for a solar-driven redox flow battery. Actually, Abruña et al.[13] and Liao et al.[11] have respectively obtained 2.8 and 1.0% efficiencies in organic/inorganic solar flow batteries providing lower energy density than VRFB, while the highest value has been reported by Li et al.,[32] with a η_{RT} of ~14.1%. Regarding solar-driven VRFB, on the other hand, Liu et al.[23] have reported 0.6% efficiency (comparative values are collected in Table S5). In fact, considering the ratio between the overall round-trip energy and the photovoltaic efficiencies, our solar VRFB with the 4CM recovers around 62% of the solar energy converted into the PV, during the discharge, which in fact confirms the suitability of this adapted module for the integration in the solar VRFB.

After considering the results we have obtained, the integration of multijunctions based on commercial photovoltaic systems demonstrates to be the most straightforward alternative for the deployment of solar redox flow batteries, from the efficiencies and costs perspectives. Additional effort must be devoted to the proper fabrication of such solar modules, but also a careful consideration of the operation performance before final integration is necessary. Although the energy storage system can also be adapted, as demonstrated by our results with the 3CM and the symmetric V4/V4 configuration, the technological development of such systems probably should go into the other direction, through the adaptation of the photovoltaic system to the needs of higher power density redox flow batteries. Besides the adaptation, alternative solutions such as using solar concentration might also contribute to advance into the attaining more realistic devices.

View Article Online
DOI: 10.1039/C9SE00949C

ARTICLE

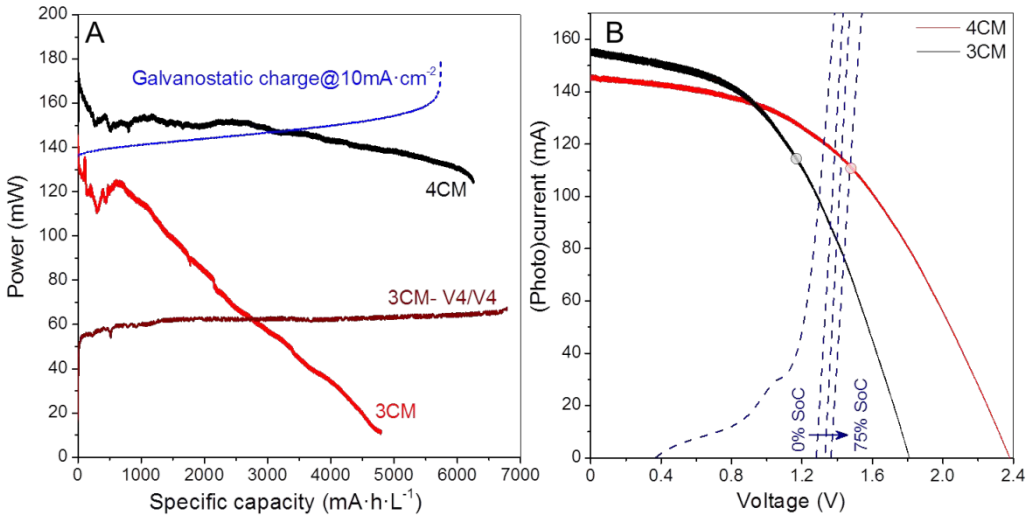

Figure 6. In (A), calculated evolution of the power during (photo)charge under different conditions: galvanostatic charge at 10 mA·cm^{-2} and photocharge with the 3CM (for full VRFB and V4/V4 configurations) and 4CM PV system under 1 Sun illumination. In (B), comparison of i-V and LSV curves for PV modules and VRFB at different SoC.

Conclusions

The integration of thin film photovoltaic modules and a full vanadium redox flow battery (VRBF) in a single straightforward device has been successfully assessed, and the influence of the intrinsic photovoltaic module on the performance has been determined. This way, a strong correlation between the photovoltaic maximum power point and the VRFB has been demonstrated, for two different Cu(In, Ga)Se_2 minimodules with 4- and 3-series-connected cells with two VRFB configurations: symmetrical V4/V4 and full VRFB. Additionally, some simple tools for correlating the performance of the photovoltaics and the battery might be found in this work.

The minimodule with 4 series-connected cells achieves full battery photocharge with round-trip energy efficiencies (~5%) among the highest ones for solar VRFB. In the case of the 3-cell module, a full dependence on the open-circuit potential of the battery was observed, leading to an excellent performance for a symmetrical V4/V4 configuration (constant power density) and to poor efficiency values in a full VRFB (decreasing power density).

Finally, we have demonstrated the tremendous potential of this kind of energy storage systems by customizing commercial thin film photovoltaics for the first time, which might shed light on the road for the future development of such solar batteries based on more simple configurations by using already existing technology.

Conflicts of interest

There are no conflicts to declare.

Acknowledgements

The authors thank Generalitat de Catalunya for financial support through the CERCA Program and M2E (2017SGR1246). IREC also acknowledges support by the European Regional Development Funds (ERDF, FEDER) and by MINECO projects ENE2016-80788-C5-5-R and ENE2017-85087-C3-2-R. S.M.-L. thanks European Union's Horizon 2020 and the Agency for Business Competitiveness of the Government of Catalonia for funding under the Marie Sklodowska-Curie grant agreement No. 712939 (TECNIOspring PLUS). M.C. thanks DOC-FAM programme (H2020-MSCA grant agreement No. 754397).

References

1 J. Jean, P.R. Brown, R.L. Jaffe, T. Buonassisi, V. Bulovic, *Energy Environ. Sci.* 2015, **8**, 1200-1219.
2 A. Gurung, Q. Qiao, *Joule* 2018, **2**, 1217-1230.
3 Z. Yang, L. Li, Y. Luo, R. He, L. Qiu, H. Lin, H. Peng, *J. Mater. Chem. A* 2013, **1**, 954-958.
4 K. Wedege, D. Bae, W.A. Smith, A. Mendes, A. Bentien, *J. Phys. Chem. C* 2018, **122**, 25729-25740.
5 S. Licht, G. Hodes, R. Tenne, J. Manassen, *Nature* 1987, **326**, 863-864.
6 H.D. Um, K.H. Choi, I. Hwang, S.H. Kim, K. Seo, S.Y. Lee, *Energy Environ. Sci.* 2017, **10**, 931-940.
7 C. Choi, S. Kim, R. Kim, Y. Choi, S. Kim, H. Jung, J.H. Yang, H.T. Kim, *Renew. Sust. Energ. Rev.* 2017, **69**, 263-274.
8 M. Skyllas-Kazacos, M.H. Chakrabarti, S.A. Hajimolana, F.S. Mjalli, M. Saleem, *J. Electrochem. Soc.* 2011, **158**, R55-R79.
9 M. Yu, W.D. McCulloch, D.R. Beauchamp, Z. Huang, X. Ren, Y. Wu, *J. Am. Chem. Soc.* 2015, **137**, 8332-8335.
10 P. Liu, Y.L. Cao, G.R. Li, X.P. Gao, X.P. Ai, H.X. Yang, *ChemSusChem* 2013, **6**, 802-806.
11 S. Liao, X. Zong, B. Seger, T. Pedersen, T. Yao, C. Ding, J. Shi, J. Chen, C. Li, *Nature Commun.* 2016, **7**, 1-8.
12 W.D. McCulloch, M. Yu, Y. Wu, *ACS Energy Lett.* 2016, **1**, 578-582.
13 J.R. McKone, F.J. DiSalvo, H.D. Abruña, *J. Mater. Chem. A* 2017, **5**, 5362-5372.
14 Q. Cheng, W. Fan, Y. He, P. Ma, S. Vanka, S. Fan, Z. Mi, D. Wang, *Adv. Mater.* 2017, **29**, 1700312.
15 C. Flox, S. Murcia-López, N.M. Carretero, C. Ros, J.R. Morante, T. Andreu, *ChemSusChem* 2018, **11**, 125-129.
16 K. Wedege, D. Bae, E. Dražević, A. Mendes, P.C. Vesborg, A. Bentien, *RSC Adv.* 2018, **8**, 6331-6340.
17 R. López-Vizcaíno, E. Mena, M. Millán, M.A. Rodrigo, J. Lobato, *Renew. Energy* 2017, **114**, 1123-1133.
18 T. Shibata, K. Takahiro, Y. Nagaoka, K. Kawase, K. Yano, *SEI Technical Review* 2013, **76**, 14-22.
19 E. Mena, R. López-Vizcaíno, M. Millán, P. Cañizares, J. Lobato, M.A. Rodrigo, *Int. J. Energy. Res.* 2018, **42**, 720-730.
20 J. Lobato, E. Mena, M. Millán, *ChemistrySelect* 2017, **2**, 8446-8450.
21 J. Azevedo, T. Seipp, J. Burfeind, C. Sousa, A. Bentien, J.P. Araújo, A. Mendes, *Nano Energy* 2016, **22**, 396-405.
22 F. Urbain, S. Murcia-López, N. Nembhard, J. Vázquez-Galván, C. Flox, V. Smirnov, K. Welter, T. Andreu, F. Finger, J.R. Morante, *J. Phys. D: Appl. Phys.* 2019, **52**, 044001.
23 Z. Wei, Y. Shen, D. Liu, F. Liu, *Sci. Rep.* 2017, **7**, 1-9.
24 S. Liao, J. Shi, C. Ding, M. Liu, F. Xiong, N. Wang, J. Chen, C. Li, *J. Energy Chem.* 2018, **27**, 278-282.
25 P.D. Matthews, P. D. McNaughter, D.J. Lewis, P. O'Brien, *Chem. Sci.* 2017, **8**, 4177-4187.
26 P. Reinhard, A. Chirilă, P. Blösch, F. Pianezzi, S. Nishiwaki, S. Buecheler, A.N. Tiwari, *IEEE J. Photovolt.* 2013, **3**, 572-580.
27 J. Ramanujam, U.P. Singh, *Energy Environ. Sci.* 2017, **10**, 1306-1319.
28 M.. Powalla, S. Paetel, D. Hariskos, R. Wuerz, F. Kessler, P. Lechner, W. Wischmann, T.M. Friedlmeier, *Engineering* 2017, **3**, 445-451.
29 C. Ros, T. Andreu, S. Giraldo, Y. Sánchez, J.R. Morante, *Sol. Energy Mater Sol. Cells* 2016, **158**, 184-188.
30 M. Chen, Y. Liu, C. Li, A. Li, X. Chang, W. Liu, Y. Sun, T. Wang, J. Gong, *Energy Environ. Sci.* 2018, **11**, 2025-2034.
31 D. Bae, G.M. Faasse, G. Kanellos, W.A. Smith, *Sustain. Energy Fuels* 2019, **3**, 2399-2408.
32 W. Li, H.C. Fu, Y. Zhao, J.H. He, S. Jin, *Chem* 2018, **4**, 1-14.
33 W.Li, E. Kerr, M.A. Goulet, H.C. Fu, Y. Zhao, Y. Yang, A. Veyssal, J.H. He, R.G. Gordon, M.J. Aziz, S. Jin, *Adv. Energy Mater.* 2019, 9, 1900918.
34 J. Vázquez-Galván, C. Flox, C. Fàbrega, E. Ventosa, A. Parra, T. Andreu, J.R. Morante, *ChemSusChem* 2017, **10**, 2089-2098.
35 W. Duan, B. Li, D. Lu, X. Wei, Z. Nie, M. Vijayakumar, J.P. Kizewski, A. Hollas, D. Reed, V. Sprenkle, W. Wang, *J. Energy Chem.* 2018, **27**, 1381-1385.
36 R.A. Potash, J.R. McKone, S. Conte, H.D. Abruña, *J. Electrochem. Soc.* 2016, **163**, A338-A344.

View Article Online
DOI: 10.1039/C9SE00949C

Adapted CIGS were integrated into vanadium redox flow batteries showing that only photovoltaics matching cell requirements achieve full unbiased photo-charge.